Chemical Engineering Science 320 (2026) 122536

Contents lists available at ScienceDirect

Chemical Engineering Science

journal homepage: www.elsevier.com/locate/ces

Bubble population growth and gas release from packed beds of AW500 ion exchange pellets

Luke Driver [a,1], Ahmad Mohamadiyeh [a,b,1], Kasia Nowakowska [a,1], Cristina Teleanu [a,1], Isabel Latimer [a,b], Gamuchirai Ashley Sibanda [b,c], Martyn Barnes [d], Michael Fairweather [b], Jeffrey Peakall [e], Timothy N. Hunter [b,*]

[a] Centre for Doctoral Training (CDT) in Fluid Dynamics, School of Computing, University of Leeds, Leeds LS2 9JT, UK
[b] School of Chemical and Process Engineering, University of Leeds, Leeds LS2 9JT, UK
[c] GREEN Nuclear CDT, University of Leeds, Leeds LS2 9JT, UK
[d] Sellafield Ltd, Hinton House, Birchwood Park Avenue, Warrington WA3 6GR, UK
[e] School of Earth and Environment, University of Leeds, Leeds LS2 9JT, UK

ARTICLE INFO

Keywords:
Cylinder packing
Gas ebullition
Gas migration
X-ray CT
Nuclear waste
Ion exchange

ABSTRACT

This paper explores the phenomenon of *in situ* generated gas retention within densely packed cylindrical ion-exchange pellets. Initially, discrete element method (DEM) simulations were used to identify pertinent contact packing parameters, rigorously validated through packing experiments. Calibrated values for dynamic and static friction, and the coefficient of restitution were found in ranges of 0.8–1.0, 0–0.2, and 0–0.2, respectively, with the importance of dynamic friction highlighted. The DEM validation process achieved a packing fraction that exhibited < 4 % deviation from experimental data, with some cylinder alignment observed near the column base. Additionally, laboratory-scale gas generation tests were conducted to replicate the retention of hydrogen within densely packed beds, achieved through the decomposition of hydrogen peroxide. X-ray computed tomography was then used to quantify bubble population size and growth within the beds. Experiments suggested a dynamic bed retention gas fraction of $\sim$7 %, which was produced within the first 30 min of generation. In parallel, CT imaging of the bubble populations indicated that large bubbles become less spherical over time, likely from pore invasion, partial cavity expansion and secondary coalescence. These mechanisms led to bubbles located in the upper portion of the bed being more likely to be released buoyantly, compared to those situated in the bed's lower regions. Overall, results indicate that the pore network channels within the pellet beds are large enough to achieve relatively steady gas release. These dynamics reduce the risk of sudden hydrogen rollover occurring industrially, particularly within the specialised context of nuclear waste management.

1. Introduction

The study of *in situ* gas generation, retention and release in packed sediment beds has witnessed significant growth in recent decades. A substantial portion of the literature concentrates on methane emissions induced by methanogenesis in natural water systems, such as lakes (Johnson et al., 2002; Wheeler, 1988) and reservoirs (Maeck et al., 2013), due to the implications between greenhouse gas emissions and climate change (Harrison et al., 2021; Katsman, 2024). However, the same mechanisms for gas retention and release, with relevance to environmental systems, are also pertinent in industrial applications. For example, similar fracture mechanics are found in studies of enhanced oil recovery (Peng et al., 2024; Fan et al., 2020), while gas ebullition in slurries or sludges is important to separation processes such as waste-water digesters (Chan et al., 2009) and flotation (Anzoom et al., 2024; Lockwood et al., 2023; Liu et al., 2025).

It is also critical in nuclear engineering, specifically when considering the safe storage and transfer of wastes that contain trapped hazardous gases, which are common at legacy sites, such as at Sellafield, UK and Hanford, USA (R. Allemann, Z. Antoniak, J. Friley, C. Haines, L. Liljegren, S. Somasundaram, Collection and analysis of existing data for waste tank mechanistic analysis, Pacific Northwest National Lab.

---

[*] Corresponding author.
E-mail address: t.n.hunter@leeds.ac.uk (T.N. Hunter).
[1] L. Driver, A. Mohamadiyeh, K. Nowakowska, C. Teleanu contributed equally to this work.

https://doi.org/10.1016/j.ces.2025.122536
Received 2 July 2025; Received in revised form 11 August 2025; Accepted 30 August 2025

(PNNL), Richland, WA (United States), 1991; Le Clere, 2011). Many of these waste deposits have been present for decades, where the presence of oscillatory bed height variations serves as a reliable indicator of continual gas generation, retention, and release within these beds. Furthermore, this phenomenon offers insights into their maximum gas retention capacity (Johnson et al., 2017; Johnson et al., 2018; Van Kessel and Van Kesteren, 2002) while a particular concern is the likelihood of sudden buoyant release events, where gas accumulates to a point where density inversion occurs. The overarching objective of research in this area is the mitigation of potential hazards associated with flammable gas retention and release from legacy nuclear waste deposits (Holborn et al., 2013; Kurniawan et al., 2022; Ryu et al., 2022; Ahmed, 2019).

Importantly, research into the determination of potential gas ebullition relevant to nuclear waste processing must be seen in the context of other fields. In general, gas entrainment and growth occurs via two competing mechanisms of initial pore invasion (forming 'reservoir' bubbles) and secondary cavity expansion (sediment displacement) (Katsman, 2024; Paulin et al., 2022), as capillary forces make it energetically costly for gas to invade narrow pore throats (Paulin et al., 2022). These systems are subject to complex dynamics from the various forces interacting between gas, liquid and solid, resulting in numerous migration structures from discrete spherical or dendritic bubbles to fluidisation or fracture of the granular medium (Varas et al., 2024). It is noted that much prior work has focused on injected gas cells, which often feature finger to fracture transitions (Varas et al., 2024; Lee et al., 2020). Alternatively, *in situ* gas generation may be more applicable to trapped methane in marine environments (Katsman, 2024), although it can be complicated due to heterogeneous nucleation and solute transport. Nevertheless, it would be expected that bubble networks generated *in situ* may be more finely distributed with higher prevalence of capillary invasion (Johnson et al., 2018; Liu et al., 2018).

The role of the sediment size and its correlation with microstructure is also critical. For many fine sediments, often their gas interaction behaviour may be simplified as a yield stress fluid (Daneshi and Frigaard, 2023; Wang et al., 2025), with the fluid thixotropy (Hou et al., 2025) and variations in fracture toughness (Katsman and Painuly, 2022; Zhou and Katsman, 2022) resulting in considerable differences in growth anisotropy. It has also been shown that variations in fine sediment clay-like microstructure can result in a substantial range in the cluster sizes of trapped bubble networks (Johnson et al., 2019). For larger granular material, the greater inertial yield stress and larger pore radii may result in higher prevalence of pore invasion as sediment size increases.

This current investigation explores the feasibility of hydrogen retention within coarse packed particle beds using zeolite AW500, an established ion exchange material typically employed in nuclear waste management (Lee et al., 2020; Wilmarth et al., 2011). It is important to note that AW500 is traditionally used for nuclear waste processing and treatment, rather than for direct gas storage applications. However, due to direct radiolysis of water, hydrogen is generated (O'Leary et al., 2021) which under certain coarse particle beds can accumulate and suddenly release (Johnson et al., 2019; Mahabadi et al., 2018; Schout et al., 2020; Suekane et al., 2010). Additionally, hydrogen can be generated via corrosion of any metallic cladding or uranium present (Paraskevoulakos et al., 2020). Hydrogen release depends on multiple factors, including particle attributes (such as shape, size, and packing) (Doraia et al., 2012; Niegodajew et al., 2022; Zhang et al., 2022), gas properties, pressure levels, flow dynamics, bed depth, and the inherent porosity and permeability of the bed. Understanding how packed AW500 pellets interact with hydrogen gas is crucial to prevent unexpected gas retention phenomena. Therefore, this investigation is essential not only to prevent unforeseen gas storage during waste treatment processes but also to contribute to our understanding of the broader applications of this material.

In this study, material shape and packing behaviour are investigated using the discrete elements method (DEM) as in (Tangri et al., 2017), with rigorous validation through packing experiments. Laboratory-scale gas generation experiments are then conducted to measure the total gas retention within densely packed beds comprising of AW500 pellets, achieved through the decomposition of hydrogen peroxide to produce oxygen *in situ*. This work is complemented by detailed advanced X-ray computed tomography (CT) imaging to observe the retained bubble populations, as applied recently to similar sediment and bubble systems (Fan et al., 2020; Anzoom et al., 2024; Liu et al., 2018), with a focus on analysing their size, growth and eventual release over time.

2. Materials and methods

2.1. Materials

In this study, AW500 cylindrical ion exchange pellets (Honeywell UOP, US) were used, matching the precise material employed in skips for pond water treatment at Sellafield Ltd., U.K. (NDA, 2007). Preliminary experiments were conducted to characterise the size and density of these pellets, with the resulting distribution depicted in Fig. 1. The average pellet length and diameter were determined to be 6.2 mm and 2.8 mm, respectively. The bulk density of the pellets was measured at 1407 kg/m^3, while the skeletal density was found to be 2157 kg/m^3 using a pycnometer. Fig. S1, within the Electronic Supplementary Material (ESM), shows a close-up image of a small pile of pellets, used to observe the natural angle of incline. Hydrogen peroxide (30–31 % w/w, Sigma-Aldrich, US) was used to generate *in situ* ebullition. This method serves as a safe and accepted analogue for the study of hydrogen generation via radiolysis, with previous research confirming that gas composition does not significantly affect gas release or retention behaviour (Boudreau et al., 2005).

2.2. Dry packing of column

For each experiment, 913 g of dry AW500 ion exchange pellets were measured and added into a 300 mm high acrylic cylinder with a diameter of 118 mm, which resulted in a fill height of ~100 mm (+/- 10 mm) depending on initial compaction. To ensure a consistent filling rate, a funnel was used, with the entry point positioned at 16.5 cm from the cylinder's base (see funnel in Fig. S1). This approach was chosen and controlled in recognition of the impact that filling rate can have on particle packing, as indicated in the literature (Zhang et al., 2022). The volume of the pellets, denoted as $V_{pellets}$, was calculated by multiplying the mass by the pellet density. The height, denoted as H, was measured with a millimetre-precision scale on the cylinder's wall. After filling, the cylinder was shaken for 3 s, and the bed height was re-measured. Both

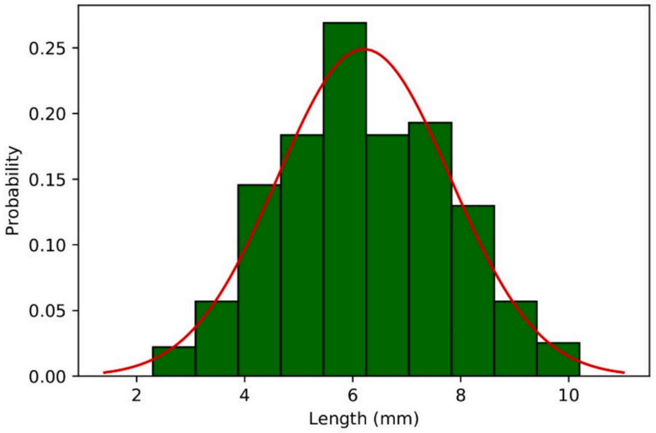

Fig. 1. Pellet length distribution obtained from 400 pellets, measured using digital callipers (0.1 mm precision).

before and after agitation, the bed volume, V_{bed}, was estimated using the formula given in Eq. (1).

$$V_{bed} = \pi r^2 H. \tag{1}$$

2.3. Gas hold-up

To investigate the gas retention fraction within a packed bed of ion exchange pellets, a series of laboratory-scale experiments were carried out, similar to those conducted by other authors (Johnson et al., 2017; Liu et al., 2016). Again, 913 g of dry ion exchange pellets were carefully added into the 118 mm diameter acrylic test cylinder and agitated for 3 s, again giving a hight of ~100 mm with an initial bed volume of ~1194 ml. To accurately gauge the bed's height, measuring approximately 10 cm, a precision scale with 1 mm accuracy was employed and mounted on the cylinder wall. Due to their highly porous nature (Ghasemi et al., 2018), the pellets were required to be submerged in deionised water for a minimum duration of 12 h prior to the experiment in order to ensure complete pellet saturation. Immediately before use, water was drained through a valve at the base of the cylinder. A close-up image of the drained column is given within the ESM (Fig. S2). This rigorous process was deemed necessary to mitigate the possibility of unaccounted-for gas introduction into the system through the pellet's pore networks. A solution was prepared by blending 10 ml of 30 % w/w hydrogen peroxide with 500 ml of deionised water (peroxide:water ratio 1:50). This solution decomposes to form water and oxygen bubbles (Eq. (2)). While there are some differences in the thermodynamic properties of oxygen to the hydrogen expected in nuclear wastes, for gases of similar solubility, composition is expected to play a relatively limited role in bubble buoyancy and their retention or release within the bed (Boudreau, 2012). As oxygen does have a slightly greater solubility, it may lead to a marginally higher propensity for bubble disproportionation, however.

$$H_2O_2(l) \xrightarrow{yields} H_2O(l) + \frac{1}{2}O_2(g). \tag{2}$$

Assuming a complete reaction, the volume of peroxide was expected to decompose to a gas volume of 1175 ml, and so a similar volume to the total volume of the bed after gas retention. The solution was added into the test vessel and subsequently sealed with a lid containing a a connection tube initially open to the atmosphere. To gauge the volume of escaped gas, $V_E(t)$, from the bed, an upturned cylinder immersed in a water bath was used to measure the volume of water displaced, where the end of the collection tube was placed upon commencement of the tests. The experiments were recorded using a HD 1080p webcam while the hydrogen peroxide underwent decomposition, which was able to monitor both the increase in column liquid level from entrained gas, as well as the volume of released gas in the collection cylinder. A schematic representation and image of this setup can be found in Fig. 2. The tests were repeated four times. The *in situ* gas generation led to the displacement of the solution from the interstitial spaces between the pellets. The retained gas, $V_R(t)$, was estimated using the increase in height of the liquid line by Eq. (3),

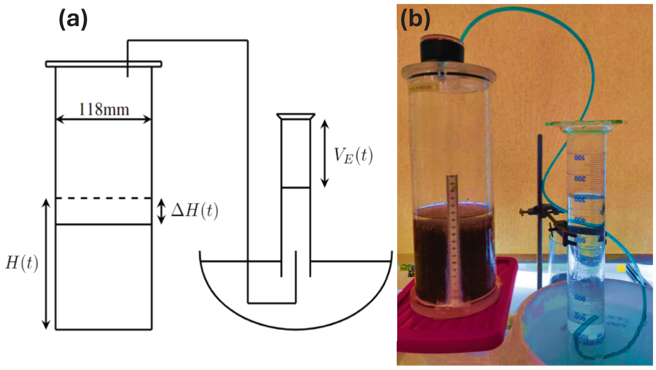

Fig. 2. (a) Schematic of the gas retention experiments, where the dashed line represents the surface of the bed at time, *t*. (b) image of filled column and gas collection during experiment.

$$V_R(t) = \pi r^2 \Delta H(t), \tag{3}$$

where $\Delta H(t)$ is the increase in the height of the solution and r is the column radius. The generated gas $V_G(t)$ can be calculated using the retained and escaped gas volumes (Eq. (4)), assuming the bed liquid is initially saturated in oxygen, and thus all O_2 produced is released as a gas.

$$V_G(t) = V_R(t) + V_E(t). \tag{4}$$

The void fraction, ε, was calculated using Eq. (5), where $V(t)$ is the instantaneous bed volume:

$$\varepsilon(t) = \frac{V_R(t)}{V(t)}.\# \tag{5}$$

2.4. X-ray computed tomography analysis

The investigation of the bubble population within the bed was carried out using a medical-grade computer tomography scanner (GE Healthcare, UK) using the parameters outlined in Table 1. Two acrylic side-on cylinders, each with a diameter of 71 mm and length of 138 mm, were employed as test vessels. The reason that a different cell configuration was required to the gas hold-up tests, was that the CT used scans horizontally rather than vertically. The cell sizes were of a smaller diameter to enable the full cells to be scanned at sufficient resolution with the CT (rather than scanning only a smaller sub-volume). The cells were packed to a relative height of ~2/3, using a 326.8 g mass of dry ion exchange pellets, which were left submerged in deionising water overnight to fully saturate the pellets. The test vessels were drained and subjected to a vacuum to remove any naturally trapped air, ensuring that the generated gas bubbles originated solely from the decomposition of hydrogen peroxide. In the first test vessel, a 175 ml volume of deionised water was syphoned into the cylinder. This vessel was scanned immediately, and again after 240 min. This vessel is referred to as the 2 phase test, aimed at investigating the packing fraction and serving as a reference for comparison. Fig. S3 within the ESM shows some example images of the cells and the CT scanner during operation and initial vacuum de-gassing.

In the second test vessel, a gas hold-up test was conducted in the same manner as described in Section 2.3. The solution was adjusted to contain 3.5 ml of hydrogen peroxide mixed with 175 ml of deionised water (and thus the same peroxide:water ratio of 1:50). This solution was pumped into the test cylinder and scanned at $t = 0$, 30, 90 and 240 min. It is noted that due to the requirement to prepare the cell and charge the peroxide outside of the CT, there was an induction time of 5 min before capturing the first CT scan, and $t = 0$ represents the point from which CT scanning occurs. This system is referred to as the three phase test and was used to investigate void fraction, bubble population and growth. The time-steps were selected based on previous gas hold-up analysis (Johnson et al., 2017).

Table 1
Brivo CT385 Imaging Parameters.

Parameter	Value
X-ray voltage (kV_p)	120
Slice separation (μm)	625
Pixel resolution (μm)	203
Voxel size (μm^3)	190 × 190 × 625
Total scan volume (mm^3)	96 × 96 × 150
Total scan volume (voxels)	512 × 512 × 240
Number of slices	240

Statistical analysis of the packing fraction and bubble populations was conducted using both two and three dimensional approaches. For each CT scan, a stack of 240 images was generated representing vertical slices through the test vessel. However, due to interference from the ends of the test vessel, image analysis was confined to the inner 200 slices, which represented the middle 125 mm of the test vessel.

Using Matlab (Mathworks, v. R2018b), the stack of images was imported as a raw radiodensity distribution in matrix form. For the two phase test, a binary mask distinguishing black solid particles from the white liquid was created. The packing fraction of each slice was defined as the area covered by solid particles over the total area of the bed, including both solid and liquid components. This calculation was based on the number of pixels. Since the liquid phase and acrylic cylinder had similar Hounsfield units (HU), direct thresholding of the entire image would incorrectly classify the cylinder as liquid phase, hence introduce errors into the packing fraction calculations. To address this issue, the centre of the test vessel was determined for each slice in ImageJ (Schneider et al., 2012), a crucial step given the slight variations in the vessel's alignment with the scanner due to its non-perpendicular positioning. Subsequently, a circular region of interest defined by the centre and radius of the test vessel was extracted, ensuring that only the inner area of the test vessel was considered for calculations.

A similar approach was applied in the three phase test for determining the void fraction in each slice. In this case, a binary mask was created to differentiate black bubbles from a white background containing both liquid solution and solid pellets. The void fraction was then calculated as the area occupied by the black bubbles over the total area of the bed, which included the solid, liquid and gas phases. An example of this sequence, showing the production of a binary image and visualised areas of extracted 3D bubbles for a particular depth slice, is given within the ESM (Fig. S4) at $t = 240$ min.

$$d_b = \sqrt[3]{\frac{6V_b}{\pi}}. \tag{6}$$

Since thresholding plays a pivotal role in image post-processing (Taina et al., 2008), a sensitivity study was conducted, for a radiodensity threshold range between 700 and 10000 HU. Analysis suggested an optimal radiodensity threshold range between 850 HU and 950 HU. At lower values, smaller bubbles went undetected as areas of grey, while higher values led to some artifacts and merging of bubbles. To illustrate these differences, Fig. 3(a)–(d) give examples of the same depth slice at $t = 30$ min with different thresholding values. Further quantitative testing revealed that varying the threshold had a negligible impact on the bubble diameter histogram, within the same range of 850 to 950 HU. The bubbles in the 50th percentile ($d_{b,50}$) and the 90th percentile ($d_{b,90}$) exhibited variations of only 4.1 % and 6.0 % respectively, as given by the distributions in Fig. 3(e).

The number of mature bubbles, defined as those larger than 5 voxels (Johnson et al., 2017), ranged between 2650 and 2799, indicating the presence of several bubbles close to pixel resolution. Ultimately, the threshold value of 900 HU was chosen (within the 850 to 950 HU range) as it did not meaningfully impact the results.

Further analysis was employed to explore the size and growth of the bubble population. For processing, ImageJ FIJI (Schindelin et al., 2012) was used, and the 3D Object Counter Fiji algorithm (Bolte and Cordelières, 2006) was employed for identifying and labelling individual bubbles. This algorithm connected voxels with the same intensity in adjacent slides, and provided object maps. From the object surface areas, A, and volume, V, the digital sphericity, Ψ_{dig}, of each bubble was estimated using Eq. (7):

$$\Psi_{dig} = \frac{6}{A}V^{\frac{2}{3}}. \tag{7}$$

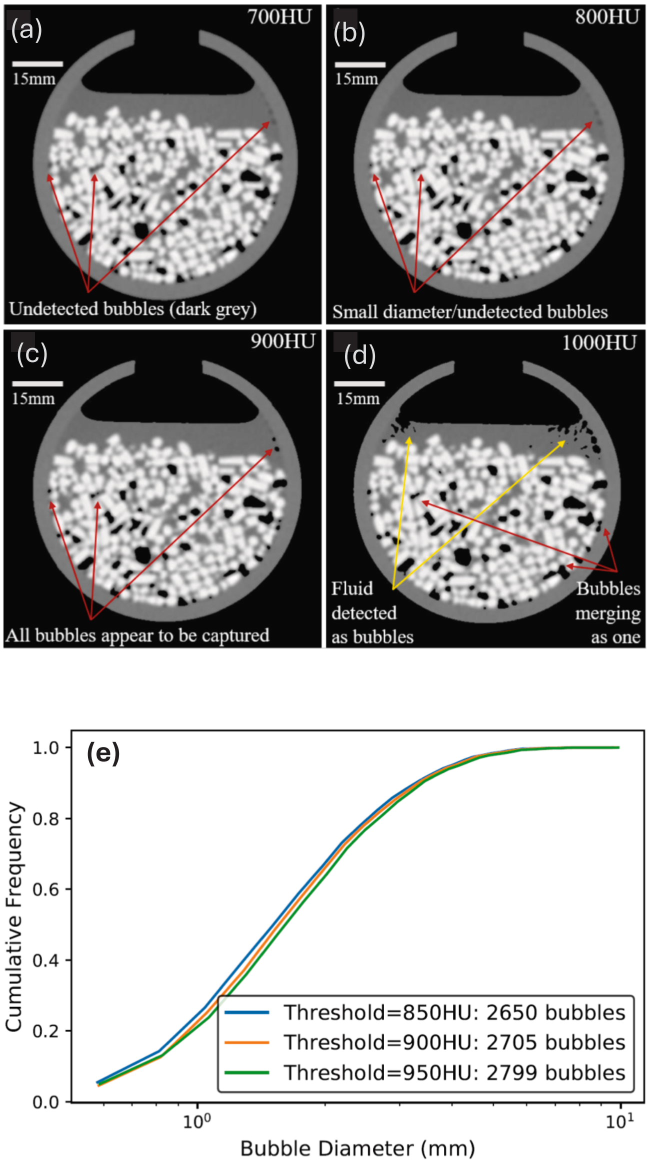

Fig. 3. (a)–(d) Example CT images showing an identical depth slice at 30 min, with different threshold radiodensity values. (e) Sensitivity of the bubble population to the threshold level at the same time.

Four thresholded stacks were concatenated to form a hyperstack, enabling the visualisation of bubble evolution over time. The 'Image Calculator' function was utilised to evaluate bed rearrangement and water level changes between the initial and final steps.

2.5. Discrete element method simulations

The discrete element method is a numerical technique employed in computational mechanics to model the behaviour of granular materials and individual particles. DEM excels at simulating the dynamics of discrete particles within large-scale systems. It places emphasis on modelling the interactions between individual particles (Zhong et al., 2016), which encompass various contact forces, including friction, cohesion, and restitution. These forces play a significant role in determining how particles respond when they come into contact. Existing literature demonstrates that these forces can influence mechanical behaviours, such as particle packing fraction and structure (Tangri et al., 2017).

DEM algorithms utilise contact detection methods to determine when particles are in contact with, or in close proximity to, one another. These algorithms are continually evolved and adapted to accommodate a wide range of non-spherical particle shapes (Höhner et al., 2011). Some are designed as general contact methods suitable for most non-spherical meshes, while others are tailored for specific shapes (Kodam et al., 2010; Kodam et al., 2010), which have been specifically adapted and validated for cylinders. Calibrating DEM variables is an essential step before proceeding with simulations to ensure the physical validity of the model (Coetzee, 2020). This calibration becomes particularly critical when working with non-spherical particles because these problems tend to be more complex, and there are fewer available resources in the literature for benchmarking validations.

Particle contact forces are split into tangential and normal parts, where $F_{ij}^{c} = F_{ij}^{n} + F_{ij}^{t}$. The forces are calculated via the linear spring dashpot method (Biegert et al., 2017; Rettinger et al., 2022), as given by Eqs. (8) and (9):

$$F_{ij}^{n} = \begin{cases} -k_n \delta_{ij} n_{ij} - \eta_n u_r^n, \delta_{i,j} > 0, \\ 0, else. \end{cases} \tag{8}$$

$$F_{ij}^{n} = \begin{cases} -\min\left(\mu\left|F_{ij}^{t}\right|, \eta_t\left|u_r^t\right|\right)\dfrac{u_r^t}{\left|u_r^t\right|}, \left|u_r^t\right| > 0, \\ 0, else. \end{cases} \tag{9}$$

Here, δ_{ij} is the overlapping distance, k_n is the spring stiffness, η represents the damping coefficient, u_r is the relative velocity, and μ is the friction coefficient.

In this DEM model, k_n accounts for the elastic part of the impact, while η accounts for the energy lost during collision. The relationship between k_n and η is given as Eqs. (10) and (11) (Michaelides et al., 2022):

$$\eta = \frac{-2\ln e_n \sqrt{mk_n}}{\sqrt{\pi^2 + \ln^2 e_n}}, \tag{10}$$

$$T_c = \frac{2\pi m}{\sqrt{4mk_n - \eta_n^2}}. \tag{11}$$

Here, e_n is the coefficient of restitution, m is the reduced mass for a particle pair (kg), and T_c is the collision time (s). After specifying a collision time, Eqs. (10) and (11) are used to compute k_n and η, which are then used to calculate the contact forces between the particles as per Eqs. (7) and (8).

2.6. DEM simulation setup

Dry granular packing simulations were carried out using the lattice Boltzmann framework WaLBerla (Erlangen, Germany) (Bauer et al., 2021) and are based on granular packing and rheology simulations (Rettinger et al., 2022). The code utilises the linear spring dash-pot model with a general contact detection algorithm for collision. Packing fraction is given by,

$$\epsilon_p = \frac{V_p}{V_t}, \tag{12}$$

where V_p is the volume occupied by particles (m^3) and V_t is the total container volume (m^3). A cylindrical container domain type, with height$H = 300$ mm and radius $r = 59$ mm was used to imitate dry packing experiments on a 1:1 basis, as seen in Fig. 4. We note the entire cylinder length was simulated (rather than the 1/3 packing height used experimentally) to extend sensitivity analysis into the influence of height on packing orientation.

Six polygonal cylindrical meshes were generated using Blender (Blender Foundation), each comprising of 200 vertices. These meshes have a uniform diameter of 2.8 mm, with the cylinder length ranging from 2 mm to 12 mm. These were imported into WaLBerla as.obj files to be used with OpenMesh (RWTH Aachen University, Germany). To ensure that the particle length distribution aligned with the data presented in Fig. 1, the unscaled meshes were applied with a fraction shape variant, using a diameter mass fraction distribution. Specific values for this diameter mass fraction distribution can be referenced in Table 2.

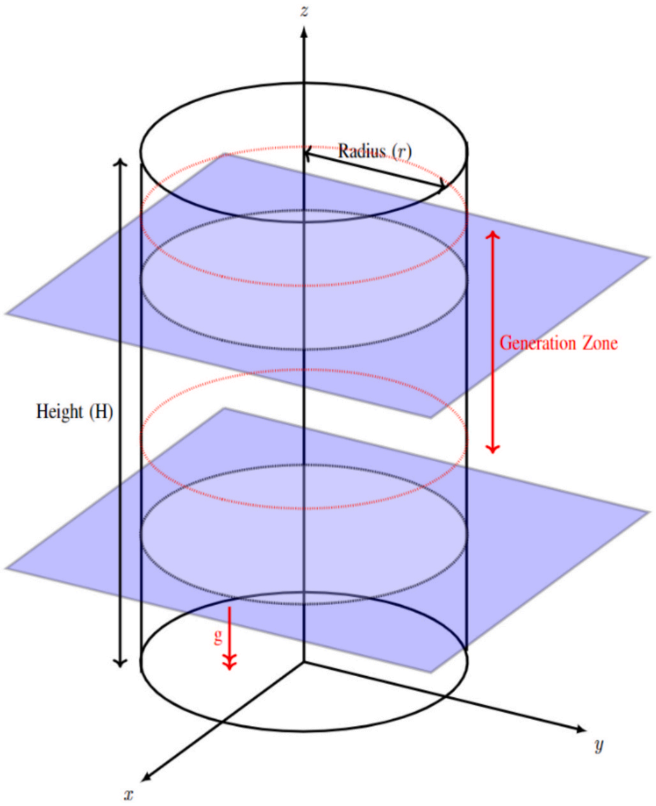

Fig. 4. Particle packing setup showing the appropriate dimensions, where g relates to direction of gravity. The packing fraction profiles are obtained from the transverse x-y planes indicated in blue. Diagram is not to scale. (For interpretation of the references to colour in this figure legend, the reader is referred to the web version of this article.)

Particle generation commenced within the upper half of the domain, specifically between 0.5H and 1.0H (see Fig. 4), in a structured Cartesian grid formation bounded by the domain. To avoid particle overlap and prevent immediate particle collisions, a particle generation spacing of 15 mm was implemented. Subsequent particle generation was confined to the region between 0.6H and 1.0H, a choice made to prevent excessive alignment of particles parallel to the bed.

The simulation employed an initial particle velocity of (0, 0, −1) m/s, without imposing a maximum velocity constraint. The initial negative vertical component was used to better mimic the experimental packing, where particles were dropped from a funnel at a small height. The mean particle density was not considered in this simulation, as existing literature suggests that density has a negligible impact on the packing fraction (Zhang et al., 2022). The total bed mass was set at 900 g, resulting in the generation of approximately 11,000 particles. After reaching the target total mass, a sinusoidal shaking phase was initiated, spanning 2.0 s, with an amplitude of 3×10^{-4} and a period of 0.025 s. The calculated Rayleigh critical timestep was determined to be 5.72×10^{-6} s. As a result, a uniform timestep of $\Delta t = 5 \times 10^{-6}$ s was selected for

Table 2
Mass fraction obtained from experimental length distribution, average pellet diameter = 2.8 mm.

Length	2 mm	4 mm	6 mm	8 mm	10 mm	12 mm
Fraction	0.0052	0.12	0.48	0.34	0.049	0.0015

all simulations, with a particle collision time of 20×10^{-6} s. The computational code was executed in parallel using MPI on a 40-core system, and the entire process required 48 h to complete.

The primary objective of these simulations was to calibrate and experimentally validate several key DEM parameters, including static friction, dynamic friction, and the coefficient of restitution (COR) (Zhang et al., 2022; Tangri et al., 2017; Coetzee, 2020), to accurately characterise the properties of the AW500 pellets. The specific parameter values utilised in the simulations can be found in Table 3.

3. Results and Discussion

3.1. Particle packing

For the beds generated via DEM, the particle orientation throughout the bed appeared to exhibit a random pattern, with no correlation to particle length. As an example, two dimensional packing slices from the DEM are shown in Fig. 5. Although it is difficult to distinguish a specific correlation, it is important to recognise that other literature has found the aspect ratio of the cylinder to have an important impact on the orientation of cylinders during packing. This was highlighted in studies by Gan and Yu (Gan and Yu, 2020) where mono-disperse packing via DEM simulation was conducted for cylinders of different aspect ratio. The results from their study found that cylinders with a low aspect ratio (diameter/length), $0.15 < D/L < 0.5$, predominantly pack in tight vertically orientated layers. Once the aspect ratio reached $D/L = 1.0$, the number of particles observed to point in the vertical direction compared to the horizontal direction was almost evenly distributed. For the larger aspect ratios, these elongated particles appear to prefer horizontal orientation, as shown in $D/L = 5.5$ simulations, which agrees with the principle of minimum gravitational potential. This horizontal packing for large aspect ratio cylinders was also observed both experimentally and computationally in (Tangri et al., 2017). When we consider the aspect ratios of our six different cylindrical meshes, the total variation of the aspect ratio, D/L, is between $0.7 < D/L < 4.3$. Accordingly, the variation in aspect ratio in the current study is consistent with previous work (Gan and Yu, 2020) with a random distribution of horizontally and vertically orientated particles observed throughout most of the domain.

One interesting aspect is the apparent self-organisation of particles when near a cylindrical wall, with evidence of directed orientation. This behaviour has been previously documented, as highlighted in prior studies (Doraia et al., 2012; Zhang et al., 2006). Furthermore, in the initial layer of particles positioned at the bottom of the bed (below the image slice shown in Fig. 5(a)) the particles had a preference for horizontal alignment with respect to the bottom wall, again consistent with previous studies (Doraia et al., 2012; Tangri et al., 2017; Gan and Yu, 2020). This orientation at the base makes physical sense in relation to its higher stability in correspondence to the principle of minimum gravitational potential. It was observed that as the size of the bed increases, the geometry of the bed surface becomes more complex, causing particles to settle into gaps with random orientations.

Packing fraction profiles were generated by capturing transverse slices at bed height intervals of 0.01 m, as depicted in Fig. 6. This relatively large interval size was chosen to be at the particle scale to capture broader structural features and trends with height, while avoiding potential oscillations and artifacts of a sub-particle scale. Notably, the packing fraction exhibits its highest values near the bottom of the column, primarily due to the prevalent horizontal structuring in this region. In general, there is also a higher packing density in the near-wall regions which leads to a radial variation in the packing density for each given slice (see Fig. 5), although such variation was difficult to quantify. Similar observations were made in (Zhang et al., 2006) and demonstrate that wall-effects can have an influence on the packing fraction and hence porosity throughout the bed.

Table 3
DEM parameters used in simulations. Here, ‘COR’ refers to coefficient of restitution, while μ_d and μ_s are the dynamic and static friction respectively.

Simulation No.	DEM parameters			
	COR	Poisson’s Ratio	μ_d	μ_s
1,2,3	0.1	0.1–0.5	0.5	0.5
4,5,6,7	0.1–0.9	0.1	0.5	0.5
8,9,10,11,12	0.2	0	0.2–1.0	0.2
13,14,15,16,17	0.2	0	0.2	0.2–1.0

Between heights of 0.02 to 0.05 m, the bulk packing fraction remains relatively consistent, with variations stemming from the inherent randomness associated with this particle packing. It is important to note that the packing fraction near the upper bed surface is approximately 20 % lower compared to other regions, as the particles in this area are freely resting. In other areas, there are also gaps within the packing structure caused by unordered particle orientation, similar to that observed previously (Doraia et al., 2012). Due to a combination of packing behaviour near walls and the variations in particle size and orientation, it is not surprising to observe that there is a slightly larger variation of interior porosity throughout the bed than would be expected in the packing of spherical particles (Coetzee, 2020; Zhang et al., 2006).

Results from the DEM sensitivity analysis are presented in Fig. 7, showing variations in average packing fraction for variations in dynamic and static friction, Poisson’s ratio and the coefficient of restitution. For example, Fig. 7(a) exhibits a reduction in packing fraction with increasing dynamic friction (μ_d), reaching a minimum value of 0.577. Particles characterised by lower dynamic friction tend to slide and reorientate more frequently over one another, resulting in an increase in the packing fraction (Rettinger et al., 2022). This effect becomes most apparent when comparing the number of particle–particle contacts at the two extremes of dynamic friction. For instance, in the cases of dynamic friction values 0.2 and 0.1, the number of contacts was approximately 16,000 and 28,000, respectively. This observation implies that a higher number of contacts corresponds to a higher packing fraction, and conversely, a lower dynamic friction leads to an increased number of particle contacts and an augmented packing fraction.

The relationship between dynamic friction and sliding particle layers is well documented for spherical particles, particularly for simulations regarding sheared granular material (Biegert et al., 2017; Dent, 1993; Luding et al., 1998), but is less well known for non-spherical particles. Our results show similar agreement with those in (Salerno et al., 2018) regarding the relationship between dynamic friction and packing fraction, although it is important to note that simulations in this paper are conducted with a different non-spherical shape, more similar to that of a rounded-edged cube.

The impact of static friction, μ_s, on the packing fraction was found to be relatively small, showing only a 0.5 % difference between $\mu_s = 0.2$ and$\mu_s = 1.0$ (Fig. 7(b)). Previous work (Jurtz et al., 2019) discussed the relationship between static friction and particle diameter to container ratio for various particle shapes. For spherical particles, static friction has a negligible impact on the packing fraction when the ratio is 6.2. However, the impact of static friction is more pronounced in systems containing cylindrical particles. This effect is still prominent at a ratio of 12, which is the maximum value analysed in this paper. In the current system, the average particle diameter to container ratio is 42.1. Therefore, it can be inferred that for cylindrical particles, larger containers are required to observe negligible impacts from static friction. However, further detailed analysis would be required to confirm this observation.

Poisson’s ratio characterises a material’s response to axial compression under an applied load. In this study, an increase in the Poisson’s ratio from 0.1 to 0.5 led to a slight decrease of 0.14 % in the packing fraction (Fig. 7(c)). Given the relatively small bed mass of 900 g used in this study, the compressive forces acting on the particles are minimal. Consequently, slight variations in packing fractions are primarily attributable to the inherent randomness of the packing, which can vary from simulation to simulation.

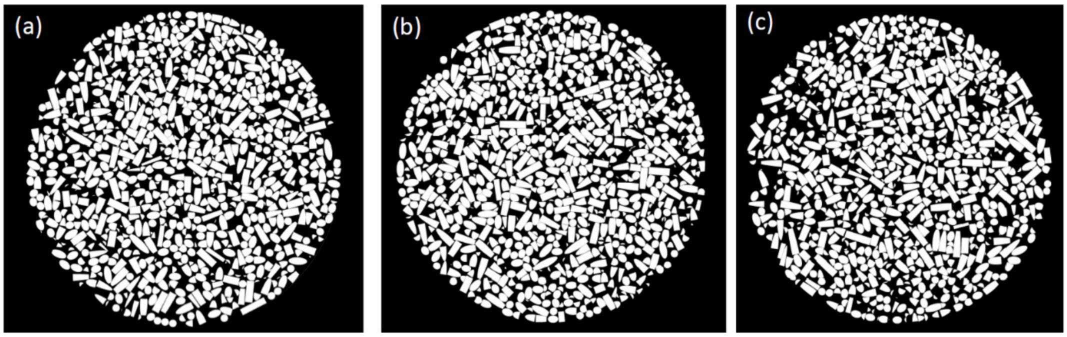

Fig. 5. Transverse slices of post-processed DEM packing simulation. White represents the AW500 pellets and black represents the voids. Here, (a) is 2 mm from the container bottom, (b) is 4 mm from the container bottom and (c) is 6 mm from the container bottom.

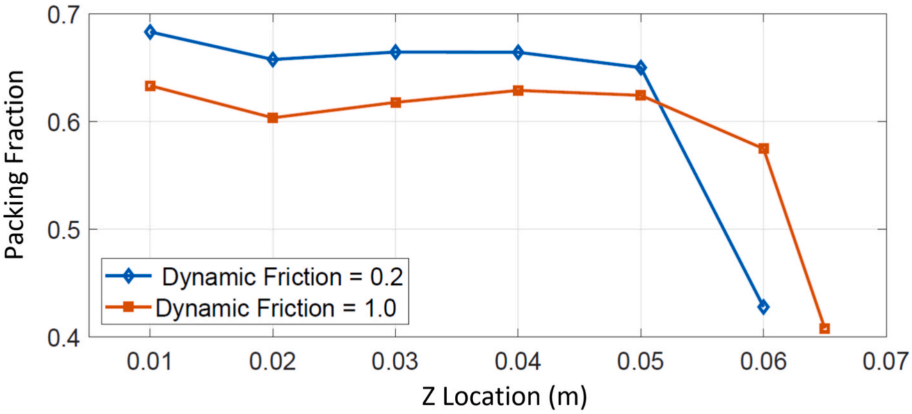

Fig. 6. DEM average simulated packing fraction profile with respect to bed height for two friction factors.

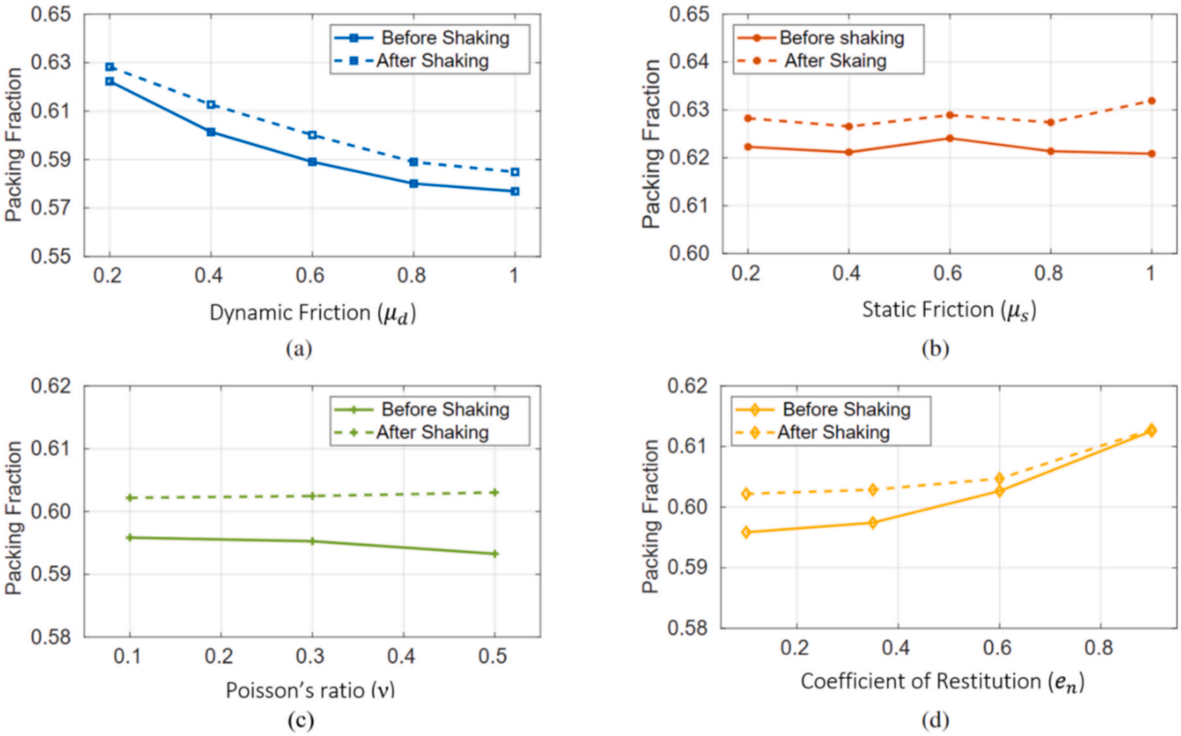

Fig. 7. Effect of DEM coefficients on packing fraction, where (a) is dynamic friction, (b) is static friction, (c) is Poisson's ratio and (d) is the coefficient of restitution.

It is important to acknowledge that Poisson's ratio can have a more pronounced impact in larger and heavier systems, as observed in the context of the Sellafield facility and detailed in the literature (Castro and Radl, 2024; Ghods et al., 2022; Pongó, 2023). In such settings, AW500 pellets can undergo crushing, potentially turning into a coarse powder even under relatively light loads. While we do not possess specific detailed information on this process, it raises the possibility that pellets located at the bottom of the skips might experience pulverisation or other forms of deformation. This compression effect arises from both the weight of the pellets and the pressure exerted by the water in the nuclear legacy waste ponds, which could lead to deviations in expected gas retention at the bottom of the bed. This consideration links back to the diverse conditions that can influence gas entrapment within coarse granular materials, as mentioned in the introduction. Factors like variations in the overhead pressure and differences in material shape and size distributions at the bottom of the zeolite skips may facilitate the accumulation of trapped gas. It is plausible that the presence of higher pressures and the subsequent reduction of the pore structures in industrial-scale applications could result in significant disparities between actual gas retention behaviour in zeolite skips and what is observed in laboratory-scale simulations. This suggestion agrees with the literature on pore-scale modelling and other techniques/observations for bubble migration and entrapment in sediments (Katsman and Painuly, 2022; Mahabadi et al., 2018; Yang et al., 2018).

The coefficient of restitution is defined as the ratio between the final and initial velocities of a particle collision. Equation (10) (see Section 2.5) illustrates the relationship between the COR and the damping coefficient, where an increase in the COR leads to a decrease in the damping coefficient. The damping coefficient serves to reduce the amount of transferable kinetic energy between particles during collisions. Consequently, a higher COR yields more energy available for particle rearrangement, ultimately increasing the packing fraction. This relationship is visually depicted in Fig. 7(d), where an increase in the COR from 0.1 to 0.9 results in a 4.1 % increase in the packing fraction. These results show strong agreement with the literature, particularly with (Wang et al., 2021) who explored the effects of COR on DEM simulated polydisperse sphere beds.

Fig. 7 also highlights the importance of the simulated shaking stage in consolidating the particle beds. The shaking stage imparts kinetic energy to the particles, enabling them to re-orientate and slide into available empty spaces. This dynamic action leads to a notable 2–3 % increase in the packing fraction for μ_d, μ_s, and ν, with no dependency on the coefficient value. However, in the COR case, the influence of shaking diminishes at higher COR values, where the kinetic energy is rapidly transferred to adjacent particles. The vibrational energy is distributed across the entire domain, lacking a distinct focus area for its impact. This accounts for the relatively minor changes in packing fraction observed at higher COR values.

As described in Section 2.2, dry packing physical experiments with the AW500 pellets were carried out using an identical domain size to the DEM. The pellets were funnelled into a 118 × 300 mm^2 measuring cylinder. The packing fraction averaged over 5 experiments was 0.561 with a standard deviation of less than 0.01. Comparing this to the DEM sensitivity analysis, the AW500 pellets can be described using $0 < e_n < 0.2$ and $0.8 < \mu_d < 1.0$. When these parameter values are applied, the predicted packing fraction aligns closely with experimental results, yielding a value of approximately 0.58. This minor discrepancy represents only a 4 % deviation from the experimental data. Regarding the static friction, preliminary pile tests resulted in an angle of repose of 41 ° (see Fig. S1) and calculated static friction of 0.87. Perhaps most importantly, the consistency in average packing and density profiles from the DEM data give confidence in the reliability of packing in the vertical column tests and smaller horizontal CT cells. Outside of some horizontal alignment in the base, general random alignment of pellets was maintained throughout the height. This result evidences our assumption that the packing profile should also be self-similar between the experimental column and the CT cells.

3.2. Gas retention experiments

The gas hold-up and release tests using 10 ml of hydrogen peroxide, H_2O_2, were repeated four times, referred to here as Tests 1–4. Fig. 8 presents (a) the total gas generated over time for the four tests, (b) the total gas hold-up in the bed, and (c) an example of the gas generated, retained and released. At 25 ° C and 1 atm, 10 ml of 30 % w/w hydrogen peroxide contains 0.098 mol H_2O_2 which decomposes to 0.049 mol O_2 (Eq. (2)). Thus, a volume of 1174 ml of oxygen was expected to be generated. However, in practice, a volume slightly greater than the expected value, 1285 ± 195 ml of oxygen was generated, shown in Fig. 8

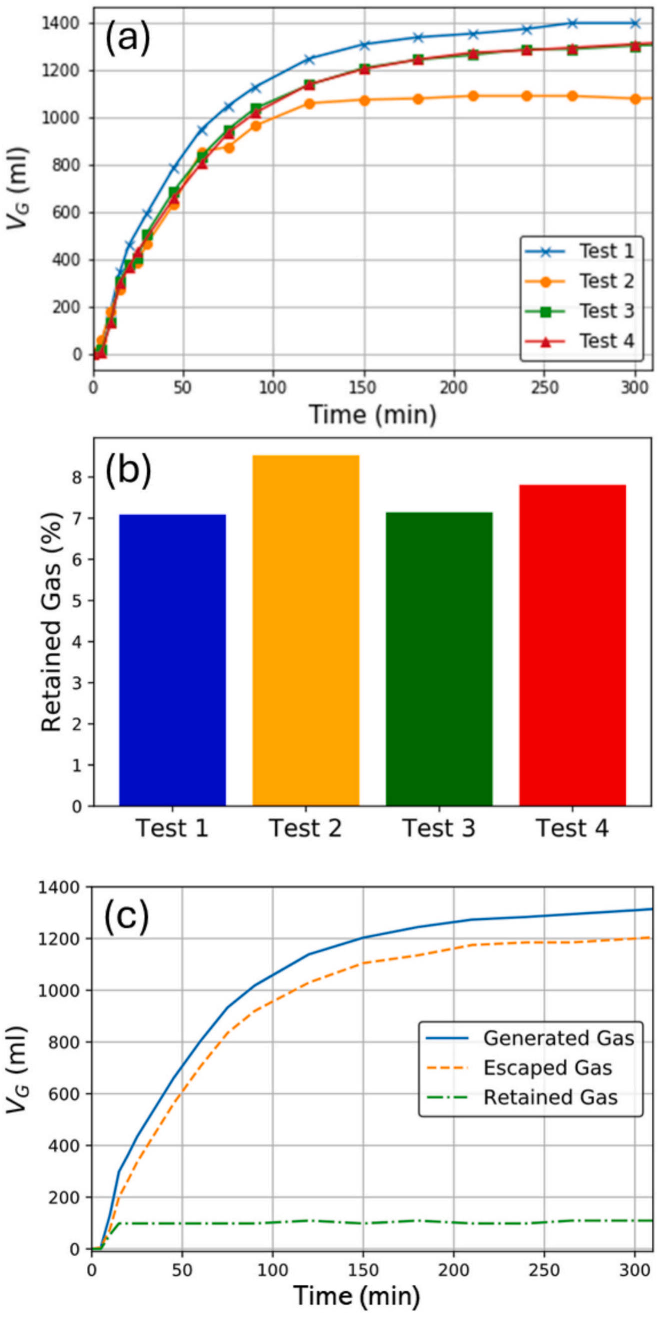

Fig. 8. (a) Gas generation profiles, (b) percentage of retained gas at 300 min for the four gas hold-up tests with 10 ml of hydrogen peroxide and (c) gas generation, retention and release profiles for Test 4.

(a).

There are two likely reasons for this discrepancy. Firstly, when the solution was added to the cylinder, air may have already been trapped within the bed of pellets which as the peroxide decomposed may have dislodged and been released as bubbles of air. Secondly, fluctuations in temperature and the precision of the syringe used to measure the peroxide can cause variation in the gas generation measurements. Indeed, between the four tests, variation in gas generation was +/- 10 %. Nevertheless, in general, there was very good consistency in the overall behaviour and level of gas retained within the beds.

Similar gas hold-up was observed for all four tests and by 300 min each bed of ion exchange pellets had a retention of 7.4 ± 0.4 % of the final gas volume, as shown in Fig. 8(b). This level indicates a relatively low maximum percentage of gas that can be held up within the AW500 ion exchange pellets, compared to prior work on cohesive nuclear waste sludges (Johnson et al., 2017; Johnson et al., 2018), at which point further gas generation results in a balanced release of bubbles. In terms of gas generation rate, the total gas production time (at ∼5 h) was also similar to previous work using peroxide decomposition (Johnson et al., 2017). The initial production rate is relatively high, due to the catalytic action of the pellets themselves, and likely above average generation from nuclear wastes (Sherwood and Eduardo Sáez, 2014) although such are situation dependent and difficult to quantify. Nevertheless, the influence of production rate on final bubble population and sizes may not be significant. Outside of extremely low generation rates (where oxygen may dissipate as dissolved gas in the liquid) bubble nucleation and growth will be influenced more through the relative heterogeneity of the surface sites on the pellets. As the volume of gas produced is far above equilibrium hold-up limit of the bed, a reduced generation rate may simply lead to longer induction times before maximum hold-up is reached.

Fig. 8(c) shows an example of the gas generation, retention, and release profiles (Test 4). Bed retention equated to 5 % of the final gas volume within the first 10 min. Maximum gas retention occurred shortly after. At this point, it appears all subsequent gas generated was released, albeit some minor fluctuations were observed where gas was temporarily retained before being released. There are two main mechanisms for the continued gas release. Either, as observed in previous work with cohesive sludge, continuous bubble networks or fissures form that act as fast release pathways (Liu et al., 2018; Johnson et al., 2019; Liu et al., 2016), or alternatively, bubbles are coalescing to a point where there is large buoyant release. Thus, X-ray CT analysis was used to investigate the bubble size and structures within the bed.

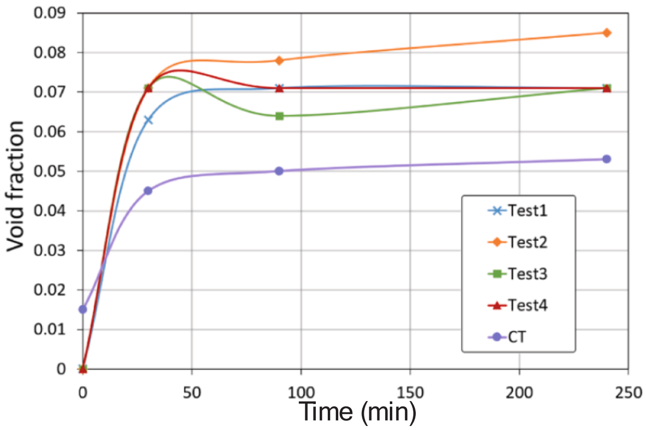

Fig. 9. Gas void fraction within the pellet beds with respect to time for the four laboratory-scale tests compared to the CT data.

3.3. *X-ray computed tomography analysis*

The void fraction for the test vessel was determined by calculating the mean value across the 200 slices. The corresponding values are presented in Fig. 9, revealing a maximum void fraction of 0.056 observed at the 240 min scan. It is essential to note ∼5 min elapsed before capturing the first CT scan, due to the requirement to prepare the cell and charge the peroxide outside of the CT, which is why the void fraction at time $t = 0$ stands at 0.015. This initial period is in alignment with the laboratory-scale retention tests where ebullition occurs within the first few minutes to tens of minutes.

As also shown in Fig. 9, the CT test exhibits a comparable gas retention profile with time to the laboratory-scale tests, notably with Test 1, although it registers lower final void fraction values. Nonetheless, as with the laboratory-scale tests, final hold-up is achieved within 60 min, with a significant majority $<$ 30 min. The discrepancy in the final gas hold-up may be partially attributed to the cell preparation outside of the CT, where some agitation on transport may have led to some additional gas release. Also, there are likely limitations from the CT voxel resolution, where small gas bubbles may not be resolved and will be missed from the calculated total void fraction (with $<$ 1 mm diameter bubbles unable to be resolved). Additionally, as discussed in Section 3.1, the packing of particles within the bed is influenced by the bed height. The relatively lower bed height combined with the horizontal orientation of the CT cell (as opposed to an upright cylinder) allowed for a higher portion of pellets to be freely resting, potentially resulting in a less densely packed bed. It is assumed that this, in turn, may have facilitated easier gas release from the pore network.

After verifying the bulk hold-up performance, the gas void fraction measured from CT was analysed to determine the spherical equivalent diameter bubble populations. Fig. 10 presents the averaged cumulative 50th percentile ($d_{b,50}$) and 90th percentile ($d_{b,90}$) bubble sizes at the four scan times (t = 0, 90, 120, 240 min). The average bubble sizes are observed to grow larger over a similar timeframe of the bulk hold-up increase, before equilibrating. As bubbles grow larger, buoyant release will become more favourable, perhaps suggesting this mechanism is responsible for defining the dynamic limit of gas hold-up in the bed.

In Fig. 11, the sphericity of the bubble populations is analysed over time, with respect to bubble count and their total volumes (inset). The average sphericity with respect to bubble count is relatively stable over time at 0.6–0.7, which suggests some elongation in bubbles is occurring due to gas bubbles exploiting pores penetrating between grains. Interestingly, when one considers changes with respect to bubble volume (Fig. 11 inset) there is a shift to less spherical bubbles over time (especially at 240 min). This change suggests behaviour may be dominated by a relatively small amount of large coalesced bubbles between the pore networks, which further elongate their average shape.

To probe the dynamics of the system further, image subtraction and hyper-stacking of the data at different times was used to assess the movement of both the pellets and the bubbles, to capture the effect of coalescence and buoyant movement. Results are illustrated in Fig. 12. In Fig. 12(a) is given the two phase (pellet liquid) displacement (with the contrast set to ignore the gas volume). The data processing involved subtracting the initial bed image from the final one, effectively illustrating the movement of pellets and the rise in water level over the 240 min observation period. It was evident that most of the pellet rearrangement occurred near the top of the bed, with minimal movement occurring in the lower section. This observation aligns with the notion that more gas bubbles are retained in the lower region of the bed. This effect is likely because bubbles either formed at the top of the bed or those that rise under buoyancy are more likely to escape, due to the lower surface stresses and relative ’free’ movement of the upper pellets.

In terms of the bubble movements (Fig. 12(b)), the precise mechanism of gas release appears to be a combination of initial pore invasion and network migration through capillary networks, along with some cavity expansion, resulting in buoyancy driven ebullition of larger

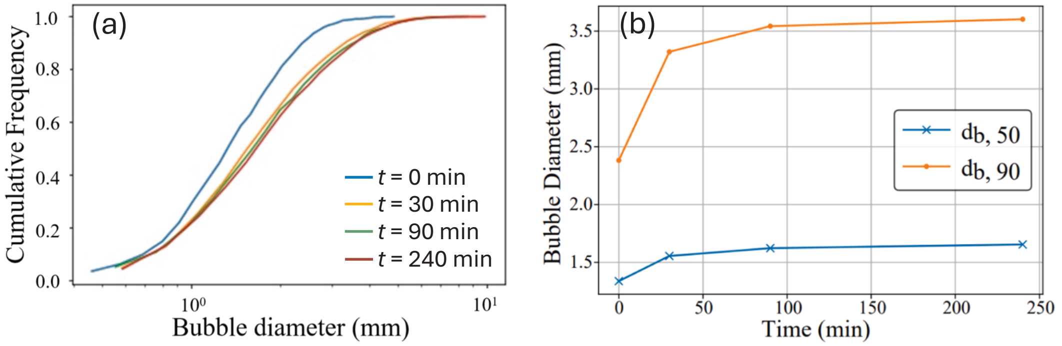

Fig. 10. Cumulative bubble distributions from CT analysis for $t = 0$, 30, 90, 240 min (a) and evolution of 50th and 90th percentile measured bubble diameters with respect to time (b).

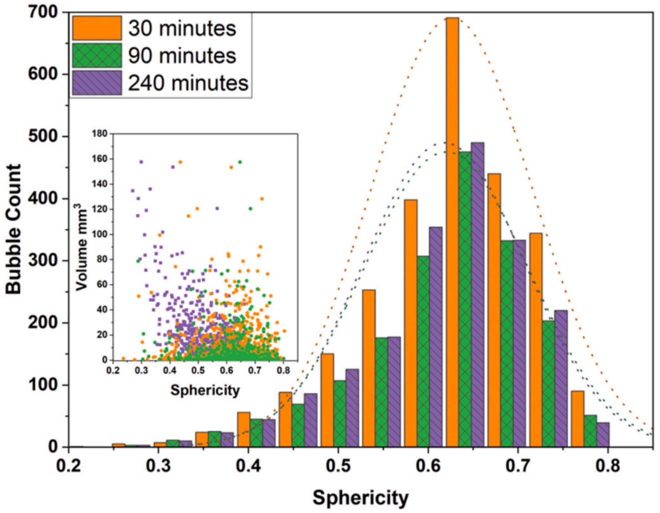

Fig. 11. Bubble volume and sphericity distribution at different times from CT analysis.

coalesced bubbles, mostly within the upper section. The evolution of bubbles throughout the stack is inconsistent, with some gas pockets expanding (labelled as α) while others are shrinking (labelled as β) in an unpredictable manner. Bubbles located along the cylinder's side appeared to migrate slightly towards the bed surface, possibly influenced by the packing behaviour along the cylinder walls. There will also be some bubble wetting behaviours (Xiao et al., 2022) caused by the different roughness of the wall in comparison to the AW500 pellets. Surface tension and gas contact angles will also play a role in the different rates of gas migration throughout the system (Lee et al., 2020; Clift et al., 2005). Unlike the DEM simulations, there appears to be a less compact packing along the edges.

Additionally, from Fig. 12(b), the bubbles in the top third of the bed that were present at either 30 or 90 min had dissipated by 240 min, confirming that once the bubbles are in the top third of the bed they are easily released from this low strength environment, due to the loose packing and movability of the pellets in the upper third of the bed. No bubbles are observed in the top third after 240 min, which suggests a quick migration once entering this region. In comparison, most bubbles at the bottom of the bed retained their location and shape throughout the whole duration of the experiment. Moreover, considering the large size of the bubbles retained by the pellets by the end of the experiment, it seems that the location of the gas pocket has more impact on the probability of being released than the diameter of the pocket. This reinforces the idea that the height of the bed is likely directly proportional

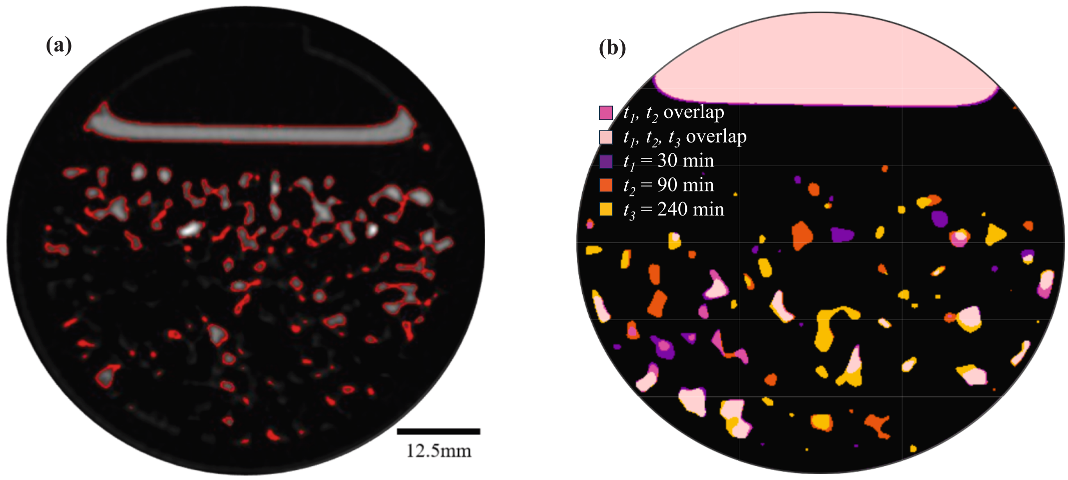

Fig. 12. X-ray tomographs showing bubble mobility. Here, (a) is the liquid–solid fluid level rise and pellets migration between $t = 0$ min and $t = 240$ min obtained through image subtraction, picturing the movement pellets and liquid at the bed surface (grey areas with red outline). Also given is (b), hyperstacked scans displaying the evolution of bubble clusters over time, including overlap areas. (For interpretation of the references to colour in this figure legend, the reader is referred to the web version of this article.)

to the percentage of gas retained by the bed. These observations are consistent with the bubble migration behaviours observed in (Johnson et al., 2017) who also evidenced enhanced bubble migration within the top third of a bed, although with cohesive magnesium hydroxide sludges.

4. Conclusions

This study investigated particle packing and gas retention in ion exchange pellet beds, of primary importance in the assessment of the hydrogen risk in nuclear storage sites (Le Clere, 2011; Ahmed, 2019). It combined discrete element modelling of column packing to inform an understanding of the void fraction and pore structure of the beds, along with experimental gas hold-up measurements and three phase X-ray CT analysis. The DEM calibration process has provided valuable insights into the recommended parameter range for the AW500 pellets employed at the Sellafield facility in the UK. Specifically, the optimised values for dynamic friction, static friction, and the coefficient of restitution fell within the ranges of 0.8–1.0, 0–0.2, and 0–0.2, respectively. The calibration process was also instrumental in achieving a packing fraction that exhibits only a minor 4 % deviation from experimental data. Also, the relative importance of the dynamic friction coefficient on equilibrium packing fractions was highlighted.

Laboratory-scale gas hold-up experiments suggested a bed retention gas fraction of ∼7 %, which builds-up largely within the first 30 min of generation. This retention is particularly significant, because it occurs while a continuous release of further gas is ongoing, suggesting a dynamic equilibrium is established where the bed is mechanically unable to retain further gas. In parallel, CT imaging of the bubble population provided critical insights, indicating that large bubbles become less spherical over time, likely from pore invasion, partial cavity expansion and secondary coalescence. These mechanisms led to bubbles located in the upper portion of the bed being more likely to be released buoyantly, compared to those situated in the bed’s lower regions. This difference in release probability is attributable to variations in packing fraction with height, underlining the importance of bed height in gas retention behaviour. Overall, results indicate that the pore network channels within the pellet beds are large enough to achieve relatively steady gas release, which should result industrially in a reduced risk of sudden hydrogen rollover events occurring.

CRediT authorship contribution statement

Luke Driver: Writing – original draft, Software, Investigation, Formal analysis, Data curation. **Ahmad Mohamadiyeh:** Writing – original draft, Software, Methodology, Investigation, Formal analysis, Data curation. **Kasia Nowakowska:** Writing – original draft, Validation, Methodology, Investigation, Data curation. **Cristina Teleanu:** Writing – original draft, Visualization, Software, Methodology, Investigation, Formal analysis, Data curation. **Isabel Latimer:** Writing – original draft, Supervision, Software, Methodology, Formal analysis. **Gamuchirai Ashley Sibanda:** Writing – review & editing, Visualization, Supervision, Investigation, Formal analysis. **Martyn Barnes:** Writing – review & editing, Supervision, Project administration, Funding acquisition, Conceptualization. **Michael Fairweather:** Writing – review & editing, Supervision, Funding acquisition, Conceptualization. **Jeffrey Peakall:** Writing – review & editing, Supervision, Resources, Conceptualization. **Timothy N. Hunter:** Writing – review & editing, Supervision, Resources, Project administration, Methodology, Conceptualization.

Declaration of competing interest

The authors declare the following financial interests/personal relationships which may be considered as potential competing interests: Luke Driver, Ahmad Mohamadiyeh, Kasia Nowakowska, Cristina Teleanu, Isabel Latimer, Gamuchirai Ashley Sibanda reports financial support was provided by Engineering and Physical Sciences Research Council. Michael Fairweather, Jeffrey Peakall, Timothy N. Hunter reports financial support was provided by Sellafield Ltd. Timothy Hunter, Michael Fairweather reports a relationship with Sellafield Ltd that includes: funding grants. If there are other authors, they declare that they have no known competing financial interests or personal relationships that could have appeared to influence the work reported in this paper.

Acknowledgements

The authors wish to thank the Engineering and Physical Sciences Research Council, UK (EPSRC) and Sellafield Ltd. for funding this work through the Centre for Doctoral Training (CDT) in Fluid Dynamics (EP/S022732/1). GA Sibanda was also supported through the Growing skills for Reliable Economic Energy from Nuclear (GREEN) CDT (EP/S022295/1). Samuel Allshorn of the University of Leeds Wolfson Laboratory is thanked for access to facilities and assistance with X-ray tomography, and Michael Johnson for support with CT analysis. Christoph Rettinger of the University of Erlangen is thanked for technical support with the waLBerla code. Numerical work was undertaken on ARC4, part of the High-Performance Computing facilities at the University of Leeds, UK.

Appendix A. Supplementary data

Supplementary data to this article can be found online at https://doi.org/10.1016/j.ces.2025.122536.

Data availability

Data will be made openly available under a Creative Commons Attribution licence (CC-BY) within the institutional White Rose Repository at DOI: https://doi.org/10.5518/1737.

References

Ahmed, F., 2019. Managing hydrogen gas hazard uncertainty. Nucl. Futur. 15 (2), 46–50.

Anzoom, S.J., Bournival, G., Ata, S., 2024. Micro-CT imaging of a frozen bubble cluster: sample holder development and image processing techniques. Sep. Purif. Technol. 335, 126111.

Bauer, M., Eibl, S., Godenschwager, C., Kohl, N., Kuron, M., Rettinger, C., Schornbaum, F., Schwarzmeier, C., Thönnes, D., Köstler, H., 2021. waLBerla: a block-structured high-performance framework for multiphysics simulations. Comput. Math. Appl. 81, 478–501.

Biegert, E., Vowinckel, B., Meiburg, E., 2017. A collision model for grain-resolving simulations of flows over dense, mobile, polydisperse granular sediment beds. J. Comput. Phys. 340, 105–127.

Bolte, S., Cordelières, F.P., 2006. A guided tour into subcellular colocalization analysis in light microscopy. J. Microsc. 224 (3), 213–232.

Boudreau, B.P., 2012. The physics of bubbles in surficial, soft, cohesive sediments. Mar. Pet. Geol. 38 (1), 1–18.

Boudreau, B.P., Algar, C., Johnson, B.D., Croudace, I., Reed, A., Furukawa, Y., Dorgan, K. M., Jumars, P.A., Grader, A.S., Gardiner, B.S., 2005. Bubble growth and rise in soft sediments. Geology 33 (6), 517–520.

Castro, F.J., Radl, S., 2024. A combined SPH-DEM approach for extremely deformed granular packings: validation and compression tests. Comput. Particle Mech. 11 (1), 185–196.

Chan, Y.J., Chong, M.F., Law, C.L., Hassell, D.G., 2009. A review on anaerobic–aerobic treatment of industrial and municipal wastewater. Chem. Eng. J. 155 (1), 1–18.

Clift, R., Grace, J.R., Weber, M.E., 2005. Bubbles, drops, and particles. Dover Publications, Mineola, NY, USA.

Coetzee, C., 2020. Calibration of the discrete element method: strategies for spherical and non-spherical particles. Powder Technol. 364, 851–878.

Daneshi, M., Frigaard, I.A., 2023. Growth and stability of bubbles in a yield stress fluid. J. Fluid Mech. 957, A16.

Dent, J., 1993. The dynamic friction characteristics of a rapidly sheared granular material applied to the motion of snow avalanches. Ann. Glaciol. 18, 215–220.

Doraia, F., Rolland, M., Wachs, A., Marcoux, M., Climent, É., 2012. Packing fixed bed reactors with cylinders: influence of particle length distribution. Procedia Eng. 42, 1335–1345.

Fan, N., Wang, J., Deng, C., Fan, Y., Wang, T., Guo, X., 2020. Quantitative characterization of coal microstructure and visualization seepage of macropores using CT-based 3D reconstruction. J. Nat. Gas Sci. Eng. 81, 103384.

Gan, J., Yu, A., 2020. DEM simulation of the packing of cylindrical particles. Granul. Matter 22, 1–19.

Ghasemi, Z., Sourinejad, I., Kazemian, H., Rohani, S., 2018. Application of zeolites in aquaculture industry: a review. Rev. Aquac. 10 (1), 75–95.

Ghods, N., Poorsolhjouy, P., Gonzalez, M., Radl, S., 2022. Discrete element modeling of strongly deformed particles in dense shear flows. Powder Technol. 401, 117288.

Harrison, J.A., Prairie, Y.T., Mercier-Blais, S., Soued, C., 2021. Year-2020 global distribution and pathways of reservoir methane and carbon dioxide emissions according to the greenhouse gas from reservoirs (G-res) model. Global Biogeochem. Cycles 35 (6), e2020GB006888.

Höhner, D., Wirtz, S., Kruggel-Emden, H., Scherer, V., 2011. Comparison of the multi-sphere and polyhedral approach to simulate non-spherical particles within the discrete element method: influence on temporal force evolution for multiple contacts. Powder Technol. 208 (3), 643–656.

Holborn, P.G., Battersby, P.N., Ingram, J.M., Averill, A.F., Nolan, P.F., 2013. Modelling the mitigation of a hydrogen deflagration in a nuclear waste silo ullage with water fog. Process Saf. Environ. Prot. 91 (6), 476–482.

Hou, Y., Jin, Z., Que, X., Zhou, Y., Zhang, Y., 2025. The influence of thixotropy on bubble growth in thixotropic yield stress fluids: insights from numerical simulations. J. Nonnewton. Fluid Mech. 335, 105353.

Johnson, B.D., Boudreau, B.P., Gardiner, B.S., Maass, R., 2002. Mechanical response of sediments to bubble growth. Mar. Geol. 187 (3–4), 347–363.

Johnson, M., Fairweather, M., Harbottle, D., Hunter, T.N., Peakall, J., Biggs, S., 2017. Yield stress dependency on the evolution of bubble populations generated in consolidated soft sediments. AIChE J 63 (9), 3728–3742.

Johnson, M., Peakall, J., Fairweather, M., Barnes, M., Davison, S., Jia, X., Clare, M.A., Harbottle, D., Hunter, T.N., 2019. Sediment microstructure and the establishment of gas migration pathways during bubble growth. Environ. Sci. Technol. 53 (21), 12882–12892.

Johnson, M., Peakall, J., Jia, X., Fairweather, M., Harbottle, D., Biggs, S., Hunter, T.N., 2018. Enhanced gas migration through permeable bubble networks within consolidated soft sediments. AIChE J 64 (11), 4131–4147.

Jurtz, N., Waldherr, P., Kraume, M., 2019. Numerical analysis of the impact of particle friction on bed voidage in fixed-beds. Chem. Ing. Tech. 91 (9), 1260–1266.

Katsman, R., 2024. Mechanics of methane bubbles in consolidated aquatic muds. Earth Sci. Rev. 257, 104908.

Katsman, R., Painuly, A., 2022. Influence of anisotropy in mechanical properties of muddy aquatic sediment on CH4 bubble growth direction and migration pattern. Eng. Geol. 299, 106565.

Kodam, M., Bharadwaj, R., Curtis, J., Hancock, B., Wassgren, C., 2010. Cylindrical object contact detection for use in discrete element method simulations Part I-contact detection algorithms. Chem. Eng. Sci. 65 (22), 5852–5862.

Kodam, M., Bharadwaj, R., Curtis, J., Hancock, B., Wassgren, C., 2010. Cylindrical object contact detection for use in discrete element method simulations, Part II—Experimental validation. Chem. Eng. Sci. 65 (22), 5863–5871.

Kurniawan, T.A., Othman, M.H.D., Singh, D., Avtar, R., Hwang, G.H., Setiadi, T., Lo, W.-H., 2022. Technological solutions for long-term storage of partially used nuclear waste: a critical review. Ann. Nucl. Energy 166, 108736.

S. Le Clere, Magnox Swarf Storage Silo Liquor Effluent Management: Sellafield Site, Cumbria, UK, International Conference on Radioactive Waste Management and Environmental Remediation, ASME, 2011, pp. 67-75.

Lee, S., Lee, J., Le Mestre, R., Xu, F., MacMinn, C.W., 2020. Migration, trapping, and venting of gas in a soft granular material. Phys. Rev. Fluids 5 (8), 084307.

Liu, J., Zhang, Y., Meng, W., Li, Z., Yang, X., Xing, Y., Gui, X., 2025. Gas dispersion properties in fluidized bed flotation columns. Phys. Fluids 37 (4), 043322.

Liu, L., De Kock, T., Wilkinson, J., Cnudde, V., Xiao, S., Buchmann, C., Uteau, D., Peth, S., Lorke, A., 2018. Methane bubble growth and migration in aquatic sediments observed by X-ray μCT. Environ. Sci. Technol. 52 (4), 2007–2015.

Liu, L., Wilkinson, J., Koca, K., Buchmann, C., Lorke, A., 2016. The role of sediment structure in gas bubble storage and release. J. Geophys. Res. Biogeo. 121 (7), 1992–2005.

Lockwood, A.P.G., Wadsley, G., Warren, N.J., Peakall, J., Webber, G.B., Wanless, E.J., Rhodes, D., Barnes, M., Harbottle, D., Hunter, T.N., 2023. Amphiphilic block copolymers as dual flocculation-flotation agents for rapid solid–liquid separation of radioactive wastes. Sep. Purif. Technol. 323, 124387.

Luding, S., 1998. Collisions & contacts between two particles. In: Herrmann, H.J., Hovi, J.-.-P., Luding, S. (Eds.), Physics of Dry Granular Media. Springer, Dordrecht, pp. 285–304.

Maeck, A., DelSontro, T., McGinnis, D.F., Fischer, H., Flury, S., Schmidt, M., Fietzek, P., Lorke, A., 2013. Sediment trapping by dams creates methane emission hot spots. Environ. Sci. Technol. 47 (15), 8130–8137.

Mahabadi, N., Zheng, X., Yun, T.S., van Paassen, L., Jang, J., 2018. Gas bubble migration and trapping in porous media: pore-scale simulation. J. Geophys. Res. Solid Earth 123 (2), 1060–1071.

Michaelides, E.E., Sommerfeld, M., van Wachem, B., 2022. Multiphase flows with droplets and particles, 3rd Edition. CRC Press, Boca Raton.

NDA, 2007 UK radioactive waste inventory, Nuclear Decommissioning Authority (NDA) Defra/RAS/08.002;NDA/RWMD/004, Moor Row, Cumbria, UK, 2008.

Niegodajew, P., Durajski, A.P., Rajca, P., Gruszka, K.M., Marek, M., 2022. Experimental and numerical study on the orientation distribution of cylindrical particles in random packed beds. Chem. Eng. J. 432, 134043.

O'Leary, M., Baidak, A., Barnes, M., Donoclift, T., Emerson, C., Figueira, C., Fox, O., Kleppe, A., McCulloch, A., Messer, D., Orr, R., Currell, F., 2021. First observation of radiolytic bubble formation in unstirred nano-powder sludges and a consistent model thereof. Sci. Rep. 11 (1), 22882.

Paraskevoulakos, C., Hallam, K.R., Adamska, A., Scott, T.B., 2020. Monitoring uranium corrosion in Magnox sludge using X-ray computed tomography: a direct analogue to "legacy" fuel storage ponds. Corros. Sci. 168, 108551.

Paulin, O.W., Morrow, L.C., Hennessy, M.G., MacMinn, C.W., 2022. Fluid–fluid phase separation in a soft porous medium. J. Mech. Phys. Solids 164, 104892.

Peng, X., Hu, Y., Zhang, F., Zhang, R., Zhao, H., 2024. A review on the water invasion mechanism and enhanced gas recovery methods in carbonate bottom-water gas reservoirs. Processes 12, 2748.

T. Pongó, Particle flows in silos, significance of particle shape, stiffness and friction: Thesis, Depósito Académico Digital de la Universidad de Navarra, 2023.

R. Allemann, Z. Antoniak, J. Friley, C. Haines, L. Liljegren, S. Somasundaram, Collection and analysis of existing data for waste tank mechanistic analysis, Pacific Northwest National Lab.(PNNL), Richland, WA (United States), 1991.

Rettinger, C., Eibl, S., Rüde, U., Vowinckel, B., 2022. Rheology of mobile sediment beds in laminar shear flow: effects of creep and polydispersity. J. Fluid Mech. 932, A1.

Ryu, J.I., Woo, S.M., Lee, M., Yoon, H.C., 2022. Ignition and flame propagation in hydrogen-air layers from a geological nuclear waste repository: a preliminary study. Nucl. Eng. Technol. 54 (1), 130–137.

Salerno, K.M., Bolintineanu, D.S., Grest, G.S., Lechman, J.B., Plimpton, S.J., Srivastava, I., Silbert, L.E., 2018. Effect of shape and friction on the packing and flow of granular materials. Phys. Rev. E 98 (5), 050901.

Schindelin, J., Arganda-Carreras, I., Frise, E., Kaynig, V., Longair, M., Pietzsch, T., Preibisch, S., Rueden, C., Saalfeld, S., Schmid, B., Tinevez, J.-Y., White, D.J., Hartenstein, V., Eliceiri, K., Tomancak, P., Cardona, A., 2012. Fiji: an open-source platform for biological-image analysis. Nat. Methods 9 (7), 676–682.

Schneider, C.A., Rasband, W.S., Eliceiri, K.W., 2012. NIH image to ImageJ: 25 years of image analysis. Nat. Methods 9 (7), 671–675.

Schout, G., Hartog, N., Hassanizadeh, S.M., Helmig, R., Griffioen, J., 2020. Impact of groundwater flow on methane gas migration and retention in unconsolidated aquifers. J. Contam. Hydrol. 230, 103619.

Sherwood, D.J., Eduardo Sáez, A., 2014. The start of ebullition in quiescent, yield-stress fluids. Nucl. Eng. Des. 270, 101–108.

Suekane, T., Zhou, N., Hosokawa, T., Matsumoto, T., 2010. Direct observation of trapped gas bubbles by capillarity in sandy porous media. Transp. Porous Media 82, 111–122.

Taina, I., Heck, R., Elliot, T., 2008. Application of X-ray computed tomography to soil science: a literature review. Can. J. Soil Sci. 88 (1), 1–19.

Tangri, H., Guo, Y., Curtis, J.S., 2017. Packing of cylindrical particles: DEM simulations and experimental measurements. Powder Technol. 317, 72–82.

Van Kessel, T., Van Kesteren, W., 2002. Gas production and transport in artificial sludge depots. Waste Manag. 22 (1), 19–28.

Varas, G., Ramos, G., Vidal, V., 2024. Interaction between gas channels in water-saturated sands. Phys. Rev. E 110 (2), 024901.

Wang, J., Lei, M., Yang, H., Xu, K., Xu, S., Zhao, P., Song, Y., 2021. Effects of coefficient of friction and coefficient of restitution on static packing characteristics of polydisperse spherical pebble bed. Particuology 57, 1–9.

Wang, S.-L., Kong, D.-Q., Tan, J.-H., Chen, Y., Zhu, B., 2025. Mechanisms driving pathway-opening migration of gas in marine clayey sediments. Eng. Geol. 348, 107965.

Wheeler, S., 1988. A conceptual model for soils containing large gas bubbles. Geotechnique 38 (3), 389–397.

Wilmarth, W.R., Lumetta, G.J., Johnson, M.E., Poirier, M.R., Thompson, M.C., Suggs, P. C., Machara, N.P., 2011. Waste-pretreatment technologies for remediation of legacy defense nuclear wastes. Solvent Extr. Ion Exch. 29 (1), 1–48.

Xiao, Y., Zheng, J., He, Y., Wang, L., 2022. Droplet and bubble wetting behaviors: the roles of surface wettability and roughness. Colloids Surf A Physicochem Eng Asp 653, 130008.

Yang, L., Ai, L., Xue, K., Ling, Z., Li, Y., 2018. Analyzing the effects of inhomogeneity on the permeability of porous media containing methane hydrates through pore network models combined with CT observation. Energy 163, 27–37.

Zhang, C., Gao, J., Xu, Y., Xia, Y., Wei, X., Su, X., Zeng, L., 2022. Void fraction for random loose packing of the cylindrical particles considering filling rate, material and shape. Particuology 63, 35–46.

Zhang, W., Thompson, K.E., Reed, A.H., Beenken, L., 2006. Relationship between packing structure and porosity in fixed beds of equilateral cylindrical particles. Chem. Eng. Sci. 61 (24), 8060–8074.

Zhong, W., Yu, A., Liu, X., Tong, Z., Zhang, H., 2016. DEM/CFD-DEM modelling of non-spherical particulate systems: theoretical developments and applications. Powder Technol. 302, 108–152.

Zhou, X., Katsman, R., 2022. Mechanical controls on methane bubble solute exchange within muddy aquatic sediments and its growth characteristics. J. Struct. Geol. 161, 104642.